Journal of Catalysis 281 (2011) 50–62

Contents lists available at ScienceDirect

Journal of Catalysis

journal homepage: www.elsevier.com/locate/jcat

Effect of the support on the high activity of the (Ni)Mo/ZrO_2–SBA-15 catalyst in the simultaneous hydrodesulfurization of DBT and 4,6-DMDBT

Oliver Y. Gutiérrez [1], Tatiana Klimova *

Facultad de Química, Departamento de Ingeniería Química, Universidad Nacional Autónoma de México, Cd. Universitaria, Coyoacán, México D.F., C.P. 04510, Mexico

ARTICLE INFO

Article history:
Received 26 January 2011
Revised 30 March 2011
Accepted 2 April 2011
Available online 6 May 2011

Keywords:
SBA-15
ZrO_2–SBA-15
Deep hydrodesulfurization
NiMoS
MoS_2
Dibenzothiophene
4,6-Dimethyldibenzothiophene

ABSTRACT

Series of Mo- and NiMo-catalysts were supported on ZrO_2, Al_2O_3, SBA-15, and ZrO_2-modified SBA-15 and tested in the simultaneous hydrodesulfurization (HDS) of dibenzothiophene (DBT) and 4,6-dimethyldibenzothiophene (4,6-DMDBT). The rate constants of the main steps in the HDS reaction network of both molecules were calculated, and the materials were characterized by N_2 physisorption, X-ray diffraction, UV–vis diffuse reflectance spectroscopy, temperature-programmed reduction and sulfidation, NO adsorption and high-resolution transmission electron microscopy. Tetrahedral and octahedral Mo species in the oxide precursors were related to the monolayers and multilayered MoS_2 structures, respectively, in the sulfide catalysts. The morphology of the active phase and the formation of the NiMoS phase were the most important factors during the HDS process of DBT-type compounds given that the turnover frequency values did not depend on the support composition or the morphology of the active phase. The monolayers of MoS_2 had low activity for the HDS of both molecules on the unpromoted catalysts, whereas on the NiMo catalysts, DBT reacted on monolayers and stacked NiMoS clusters but 4,6-DMDBT was converted only on the later structures. The optimum active phase–support interaction strength on ZrO_2–SBA-15 materials led to the characteristics of the active phase that maximized the total active surface and the active surface not sterically hindered by the support, i.e., stacked MoS_2-like clusters with short lengths. Thus, the NiMo/ZrO_2–SBA-15 catalyst was able to convert DBT-type compounds with typical and low reactivity on the NiMo/Al_2O_3 catalyst.

1. Introduction

The requirements that a fuel must meet in transport applications have become more stringent in the last decade. The concentration of sulfur, a major impurity in crude oil, has been limited to few parts per million in many countries. However, removing sulfur from diesel by the standard hydrodesulfurization (HDS) process is a major challenge because of the presence of low reactivity compounds so-called refractory. The response of refineries to the demand of high-quality diesel has been to increase the severity of the process conditions or to implement several reaction stages [1]. Sulfur is removed from the most reactive species in the first reactor or catalytic bed, whereas the refractory compounds react in subsequent stages on a second catalyst or at different conditions. However, the use of catalysts active in the HDS of refractory compounds is a more convenient option to improve the entire HDS process because it minimizes the investment needed to upgrade the product. Thus, the fundamental study of the interaction between the sulfur containing molecules and the catalysts has been the aim of many groups in the last years. The understanding of this issue would allow designing catalysts able to remove sulfur from refractory and not refractory compounds in a single reaction stage.

It is possible to use novel supports, active phases, promoters, or additives to upgrade the performance of the HDS catalyst, typically MoS_2 supported on alumina and promoted with Co or Ni [2–5]. The use of an alternative material as carrier is a promising option because the support has a key effect in the catalytic performance. A diversity of materials has been tested as HDS supports, i.e., pure oxides, mixed oxides [6–12], carbon [13], and mesostructured silicas such as MCM-41 and SBA-15 [14–19].

The application of mesostructured silicas as HDS supports is of special interest due to their outstanding textural characteristics, e.g., pore volume and surface area [20]. Pure siliceous mesostructured materials were successfully applied as supports for W and Mo catalysts in the HDS of dibenzothiophene (DBT) and thiophene and hydrogenation of cyclohexene [18,21]. It was shown afterward that adding metal oxides to the mesostructured silica led to more active catalysts for the same reactions [22]. The use of pure siliceous and modified SBA-15 materials as HDS supports has been

* Corresponding author. Fax: +52 55 56225371.
E-mail address: klimova@servidor.unam.mx (T. Klimova).
[1] Present address: Lehrstuhl II für Technische Chemie, Department Chemie, Technische Universität München, Garching, Germany.

0021-9517/$ - see front matter © 2011 Elsevier Inc. All rights reserved.
doi:10.1016/j.jcat.2011.04.001

extensively studied by our group. Mo and NiMo catalysts supported on SBA-15 materials modified with Ti, Zr or Al showed high activity in the HDS of 4,6-dimethyldibenzothiophene (4,6-DMDBT) [23–26]. NiMo catalysts supported on SBA-15 modified with different metal oxides (MgO, CaO, BaO, TiO_2, or ZrO_2) were tested in the HDS of DBT [27]. The common observation in previous works was that adding ZrO_2 to the SBA-15 led to the most remarkable improvement in the activity of the catalysts in the HDS of both DBT-type compounds, which was correlated with the morphology of the active phase.

It was interesting that the same system presented the highest activity for the HDS of DBT and 4,6-DMDBT because some studies suggested that improving the activity of the Mo-based catalysts for the HDS of DBT decreases the activity in the HDS of 4,6-DMDBT and vice versa [28]. For instance, incorporating SiO_2 to the alumina support decreased the activity in the HDS of DBT but led to higher activity in the HDS of 4,6-DMDBT [29,30]. Thus, the aim of this work was to understand the high HDS activity of the (Ni)Mo/ZrO_2–SBA-15 system by combining detailed physicochemical characterization of the catalysts with the kinetics of the simultaneous HDS of DBT and 4,6-DMDBT. Mo- and NiMo catalysts supported on Al_2O_2, ZrO_2, and SBA-15 were also investigated to achieve the goal.

The materials were characterized by N_2 physisorption, X-ray diffraction (XRD), UV–vis diffuse reflectance spectroscopy (DRS), temperature-programmed reduction and sulfidation (TPR and TPS), high-resolution transmission electron microscopy (HRTEM), and adsorption of NO. The catalytic performance of the sulfide catalyst was evaluated in the simultaneous HDS of DBT and 4,6-DMDBT. The results showed a qualitatively clear relationship between the oxide and sulfide form of the catalysts explained in terms of support-active-phase interaction strength. Furthermore, the analysis provided quantitative evidence of the key role of the MoS_2 phase morphology in the performance of the catalysts. The (Ni)Mo/ZrO_2–SBA-15 system is postulated as an alternative catalyst to remove sulfur from refractory and non-refractory compounds in a single reaction stage.

2. Experimental

2.1. Support and catalyst preparation

SBA-15 was synthesized according to the procedure reported in literature [31]. The triblock copolymer Pluronic P123 (M_{av} = 5800, $EO_{20}PO_{70}EO_{20}$) and tetraethyl orthosilicate (⩾99%, Aldrich) were used as structure-directing agent and silica source, respectively. ZrO_2-modified supports were prepared by incipient wetness impregnation of the siliceous SBA-15 with solutions of zirconium (IV) propoxide (70 wt.% in 1-propanol, Aldrich) in dry ethanol (Aldrich, 99.999%). The solids were dried at room temperature and treated in static air at 823 K for 5 h after impregnation. In the following, modified materials are referred as $ZrO_2(x)$SBA where x is the weight% loading of ZrO_2 in the parent SBA-15. Pure ZrO_2 was prepared using $ZrOCl_2{\cdot}8H_2O$ (99%, Aldrich) and ammonium hydroxide solution (28% in H_2O, Sigma–Aldrich) as reported by Jia et al. [7]. Alumina (γ-Al_2O_3) was prepared by thermal treatment of pseudo-boehmite Catapal B in air at 973 K for 4 h.

Mo and NiMo oxide precursors were prepared by successive impregnation of aqueous solutions of ammonium heptamolybdate (99.98%, Sigma–Aldrich) and nickel nitrate (⩾98.5%, Sigma–Aldrich) on the supports. The materials were treated in air at 373 K for 24 h and then at 773 K for 4 h after each impregnation. The nominal compositions were 12.4 wt.% of MoO_3 for Mo catalysts and 12 wt.% of MoO_3 and 3 wt.% of NiO for NiMo catalysts. Hereafter, the catalysts are denoted as (Ni)Mo/*support*.

2.2. Support and catalyst characterization

N_2 adsorption–desorption isotherms were measured with a Micromeritics ASAP 2000 automatic analyzer at liquid N_2 temperature. The samples were degassed ($p < 10^{-1}$ Pa) at 543 K for 6 h prior to the experiments. Specific surface areas were calculated by the BET method (S_{BET}), and the micropore area (S_μ) was estimated using the correlation of t-plot method. XRD patterns of the oxide precursors were recorded in a Siemens D5000 diffractometer, using Cu Kα radiation (λ = 0.15406 nm) and a goniometer speed of $1^\circ(2\Theta)$ min^{-1}. UV–vis electronic spectra of the samples were recorded using a Varian Cary 100 spectrophotometer equipped with a diffuse reflectance attachment. Polytetrafluoroethylene was used as reference. TPR experiments were carried out in a Micromeritics AutoChem II 2920 automatic analyzer equipped with a TCD detector. For the TPR experiments, the samples were pretreated *in situ* at 673 K for 3 h under synthetic air flow and cooled down to room temperature under Ar stream. The reduction step was performed with an H_2/Ar mixture with a heating rate of 10 K min^{-1} from room temperature to 1273 K.

For the TPS experiments, a sample of the oxide precursor was loaded in a quartz reactor and heated at 5 K min^{-1} to 673 K in a mixture of 10 vol.% H_2S/H_2. The gases evolved were monitored with a mass spectrometer (QME 200, Pfeiffer Vacuum). After the TPS experiments, the corresponding XRD patterns of the freshly sulfided catalysts were recorded in a Philips X'Pert Pro System (Cu Kα1-radiation, 0.154056 nm) using a step size of $0.017^\circ(2\Theta)$ and 115 s as count time per step.

HRTEM studies of the sulfided catalysts were carried out using a Jeol 2010 microscope (resolving power 1.9 Å). The solids were ultrasonically dispersed in heptane, and the resulting suspensions were collected on carbon-coated grids. The slab length and layer-stacking distributions of MoS_2 clusters in each sample were determined from the measurement of at least 300 crystallites detected on several HRTEM pictures taken from different places of the microscope grids. The concentration of adsorbed NO on the sulfide catalysts was determined in a flow apparatus equipped with a quartz reactor and a mass spectrometer as detector (QME 200, Pfeiffer Vacuum). Samples of 0.1 g of each oxide precursor were activated *in situ* in 10 vol.% H_2S/H_2 at 673 K for 3 h. After flushing the reactor with He for 5 h at 300 K, pulses of 10 vol.% of NO/He were introduced periodically. The concentration of gas adsorbed was calculated as the sum of the uptakes per pulse.

2.3. Catalytic activity

The catalysts were sulfided *ex situ* in a tubular reactor at 673 K for 4 h in a stream of 15 vol.% of H_2S in H_2 under atmospheric pressure prior to the activity evaluation. The particle size of the samples was 105–149 μm to avoid effects of internal diffusion. The simultaneous HDS of DBT and 4,6-DMDBT was performed in a batch reactor (Parr) at 573 K and 7.3 MPa total pressure for 8 h. The reactant solution consisted of DBT and 4,6-DMDBT in hexadecane, with sulfur concentration of 1300 and 500 ppm in DBT and 4,6-DMDBT, respectively. The reactor was charged with 40 ml of the reactant solution and 0.15 g of freshly sulfided catalyst transferred under inert atmosphere to the reactor in each run. The course of the reaction was followed by withdrawing aliquots periodically and analyzing them on an HP-6890 chromatograph with a HP-1 column.

2.4. Kinetic analysis

The HDS of DBT-type compounds occurs through the two parallel reactions illustrated in Fig. 1: direct desulfurization (DDS) yielding the corresponding substituted biphenyl products (species "*b*")

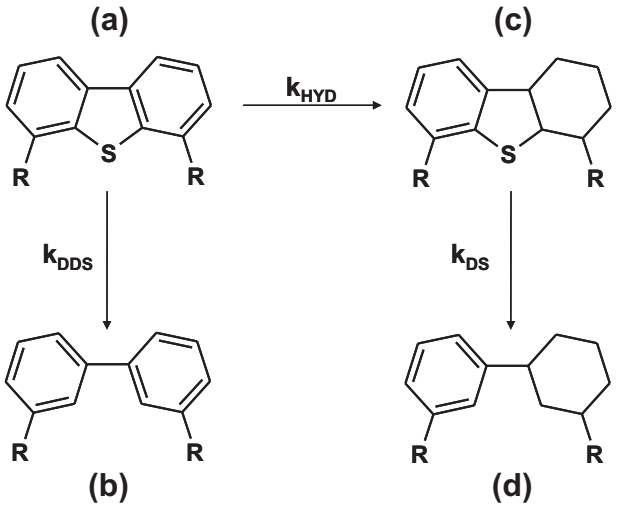

Fig. 1. Reaction network for the HDS of DBT-type compounds. R=H, for DBT; R=CH_3 for 4,6-DMDBT.

and hydrogenation (HYD) with subsequent desulfurization (DS), yielding first hydrogenated intermediates (species "*c*") and then cyclohexylbenzene-type compounds (species "*d*") [32,33]. Since the early works of Houalla et al. [34], the assumption of first-order kinetics has been especially useful in the study of HDS reactions. Indeed, the first-order expressions fit experimental results better than the Langmuir–Hinshelwood equations in the HDS of model molecules (DBT) [35]. Thus, in this work, the results of the activity tests are analyzed by applying a pseudo-first-order kinetics approach to the reaction network presented in Fig. 1. Reversibility in the HYD route and the hydrogenation of the biphenyl compounds are not considered because they are negligible at low conversions and high rates of sulfur extraction from the hydrogenated intermediates [36–39].

The equation system corresponding to the reaction network of Fig. 1 is presented in Eqs. (1)–(4), where r_i and C_i are the reaction rate and the molar concentration of species i; k_n is the pseudo-first reaction rate constant of the step n according with Fig. 1. This equation system has one set of kinetic constants that fit the experimental data and offers the possibility of analyzing the three most important steps in the HDS of DBT-type compounds, i.e., direct desulfurization (k_{DDS}) or hydrogenation (k_{HYD}) of the starting compound and the sulfur removal from the hydrogenated intermediates (k_{DS}). The experimental data from the simultaneous HDS of DBT and 4,6-DMDBT are used to numerically fit the reaction rate constants; only the results at conversions below 35% of DBT or 4,6-DMDBT are considered.

$$r_a = -(k_{HYD} + k_{DDS})C_a \quad (1)$$

$$r_b = k_{DDS}C_a \quad (2)$$

$$r_c = k_{HYD}C_a - k_{DS}C_c \quad (3)$$

$$r_d = k_{DS}C_c \quad (4)$$

3. Results

3.1. Characterization of oxide precursors

The effect of the ZrO_2 loading into the structure of SBA-15 by incipient wetness impregnation has been described in previous works [25,40]. The characteristics of Mo and NiMo catalyst supported on ZrO_2–SBA-15 modified by chemical grafting (ZrO_2 loadings <25 wt.%) were discussed in [41,42]. The application of impregnated ZrO_2–SBA-15 as HDS support was studied only for NiMo catalysts in [25]. Here, we report the characterization results that complement previous collaborations and allow us to describe the Mo and NiMo materials in the oxide state (denoted as oxide precursors).

Table 1
Textural characteristics of supports and oxides precursors. Surface area (S_{BET}) and micropore area (S_μ) in $m^2\ g^{-1}$.

	Support		Mo		NiMo	
	S_{BET}	S_μ	S_{BET}	S_μ	S_{BET}	S_μ
SBA-15	826	135	602	75	543	65
ZrO_2(25)SBA	581	105	400	55	374	32
ZrO_2(37)SBA	505	75	346	35	317	25
ZrO_2(50)SBA	391	65	283	32	244	15
ZrO_2	58	5.9	54	2.3	58	1
γ-Al_2O_3	199	0	191	0	185	0

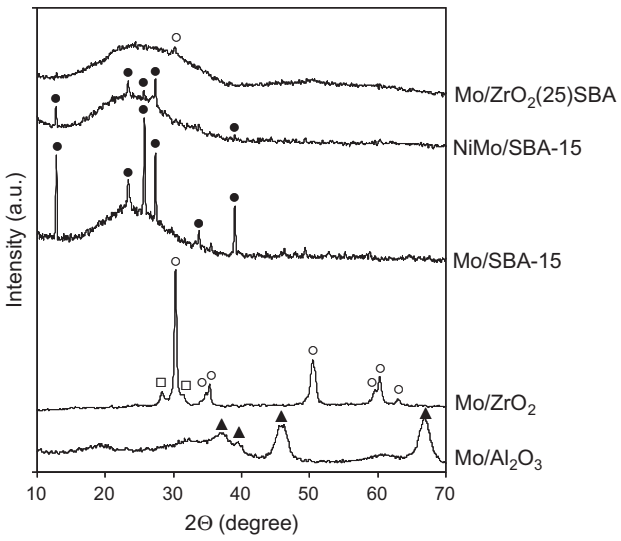

Fig. 2. XRD patterns of Mo/Al_2O_3, Mo/ZrO_2, Mo/SBA-15, NiMo/SBA-15, and Mo/ZrO_2(25)SBA. (▲) γ-alumina (JCPDS card 29-0063); (○) tetragonal ZrO_2 (JCPDS card 17-0923); (□) monoclinic ZrO_2 (JCPDS card 37-1484); (●) orthorhombic phase of MoO_3 (JCPDS card 35-609).

Siliceous SBA-15, ZrO_2, Al_2O_3, and SBA-15 modified with ZrO_2 loadings of 25, 37, and 50 wt.%, were synthesized and subsequently utilized as supports for Mo and NiMo catalysts. The main textural properties of supports and the corresponding oxide precursors are shown in Table 1. In the following, only the results for the oxide precursors supported on ZrO_2(25)SBA are given as representative of the (Ni)Mo/ZrO_2(*x*)SBA materials.

The powder XRD patterns of Mo oxide precursors supported on ZrO_2, Al_2O_3 or ZrO_2(*x*)SBA materials did not show the presence of any crystalline Mo phase (Fig. 2). The peaks in Mo/ZrO_2 belonged to a mixture of monoclinic (JCPDS card 37-1484) and tetragonal ZrO_2 (JCPDS card 17-0923). The peaks corresponded to the expected γ-Al_2O_3 structure in Mo/Al_2O_3, (JCPDS card 29-0063). In Mo/ZrO_2(25)SBA, the broad peak between 15° and 35°(2Θ) was attributed to amorphous silica whereas the signal at 31°(2Θ), and others not visible in Fig. 2 due to the scale were assigned to tetragonal ZrO_2. The Mo precursor supported on SBA-15 exhibited diffraction peaks corresponding to orthorhombic MoO_3 (JCPDS card 35-609). The intensity of these signals diminished after the addition of Ni (see Fig. 2). The average size of the MoO_3 crystals,

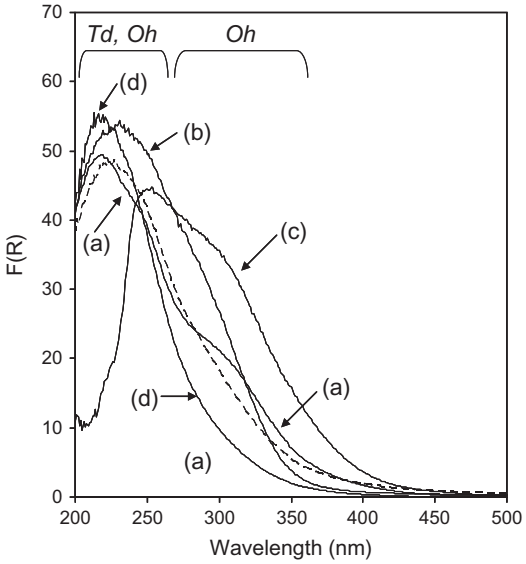

Fig. 3. DRS UV–vis spectra of Mo precursor supported on: SBA-15 (a); Al_2O_3 (b); ZrO_2 (c); and ZrO_2(25)SBA (d). The dotted line gives the spectra of the NiMo/SBA-15 catalyst.

determined using Scherrer equation, was 95 nm for Mo/SBA-15 and 52 nm for the corresponding Ni-promoted catalyst. XRD patterns of others NiMo precursors were omitted because they were identical to the patterns of the corresponding Mo precursors.

UV–vis DRS spectra of Mo and NiMo oxide precursors were recorded to obtain further information concerning the dispersion of Mo oxide species on the supports. Fig. 3 shows the spectra of selected catalysts after subtracting the spectra of the corresponding support. Hence, the adsorption bands observed in the spectra were produced only by the ligand-to-metal charge transfer $O^{2-} \rightarrow Mo^{6+}$. The position of the absorption bands was determined by the coordination and agglomeration degree of the Mo species in the sample. The bands in the range 260–280 and 300–320 nm were assigned to the isolated molybdate tetrahedral (T_d) and polymolybdate octahedral (O_h) Mo species, respectively [43–45]. The absorption bands of O_h species shifted to higher wavelengths with increasing agglomeration, e.g., bulk MoO_3 absorbs at 300–330 nm. T_d and O_h Mo species showed a second absorption band around 230 nm.

The DRS spectra of Mo precursors (Fig. 3) showed that mixtures of T_d and O_h Mo species were present in all cases, although the proportion depended on the support. In the spectra of the Mo precursor supported on SBA-15, ZrO_2 or Al_2O_3, absorption in the region 300–330 nm produced bands that were not present in the spectrum of ZrO_2(25)SBA. In the later material, the absorption band was well defined and had a maximum at 230 nm. Hence, heterogeneous distributions of O_h Mo species in several degrees of agglomeration were obtained on pure oxides, whereas supporting Mo on ZrO_2(25)SBA increased the dispersion of O_h molybdenum species. The absorption edges (E_g) calculated for Mo/ZrO_2 and Mo/Al_2O_3 were 3.4 and 3.5 eV, respectively. The absorption edges were around 4.1 on ZrO_2(x)SBA. These values confirmed that a significantly better dispersion of Mo species took place on the Zr-modified SBA-15 materials.

The addition of Ni to the materials had appreciable influence only on SBA-15 as shown in Fig. 3 (for clarity, spectra of other NiMo precursors were omitted). The absorption edge of the Mo/SBA-15 catalyst was 3.7 eV. After Ni addition, a shift of the band-gap absorption edge to 4.2 eV was observed pointing to a significant effect of Ni on the dispersion of Mo precursor supported on SBA-15.

The TPR profiles for Mo oxide precursors are shown in Fig. 4. On siliceous SBA-15, the low-temperature reduction peak observed at 763 K is ascribed to the first reduction step ($Mo^{6+} \rightarrow Mo^{4+}$) of polymeric O_h Mo species [45,46]. The H_2 consumption is constant from 823 K to 990 K and then declines gradually to the base line at 1273 K. This broad H_2 consumption region can be produced by the overlapping of the reduction of crystalline MoO_3 species (873–900 K), the second step of reduction of the polymeric O_h Mo species ($Mo^{4+} \rightarrow Mo^0$) and the first step of reduction of T_d Mo species [43,44]. Reduction of Mo species supported on ZrO_2(x)SBA materials takes place in a narrow temperature region and produced better defined signals. Fig. 4 shows the reduction profile for Mo/ZrO_2(x)SBA, and the low temperature peak (first reduction step of O_h Mo species) is observed at 733 K. The second reduction step of O_h species and the reduction of T_d Mo species are limited to

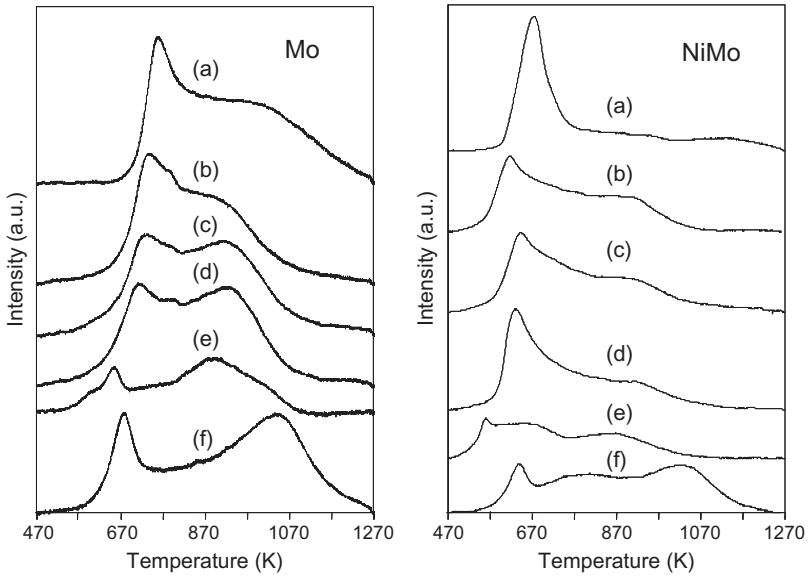

Fig. 4. TPR profiles for Mo and NiMo oxide precursors supported on: SBA-15 (a); ZrO_2(25)SBA (b); ZrO_2(37)SBA (c); ZrO_2(50)SBA (d); ZrO_2 (e); and Al_2O_3 (f).

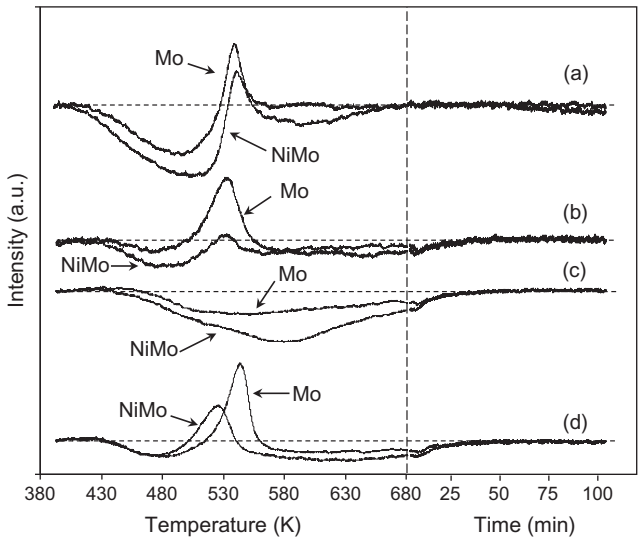

Fig. 5. H_2S profiles observed in the TPS experiments of Mo and NiMo catalysts supported on the following: SBA-15 (a); ZrO_2(25)SBA (b); ZrO_2 (c); and Al_2O_3 (d).

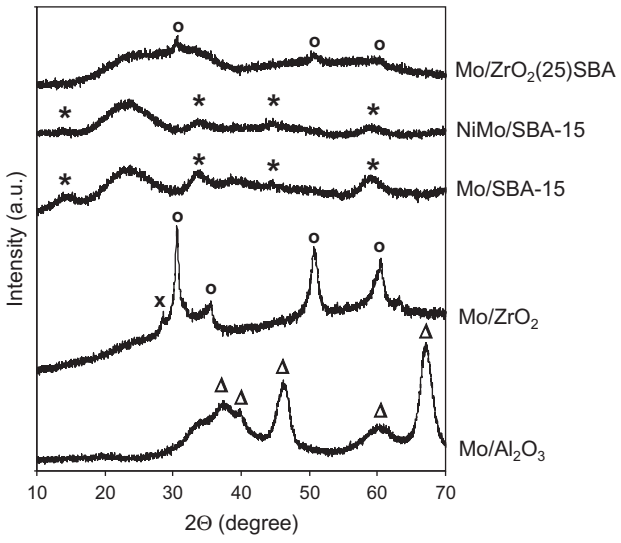

Fig. 6. XRD patterns of sulfided Mo/Al_2O_3, Mo/ZrO_2, Mo/SBA-15, NiMo/SBA-15 and Mo/ZrO_2(25)SBA. (Δ) γ-alumina (JCPDS card 29-0063); (○) tetragonal ZrO_2 (JCPDS card 17-0923); (×) monoclinic ZrO_2 (JCPDS card 37-1484); (∗) MoS_2 (JCPDS card 37-1492).

temperatures below 1073 K where a defined maximum is observed at 923 K.

Increasing loadings of ZrO_2 in the support slightly shift the position of the first reduction peak to lower temperatures and increase the intensity of the second reduction peak. The same temperature regions can be distinguished on ZrO_2 and Al_2O_3; the intensity of the reduction signal at high temperature, however, points to a higher proportion of T_d Mo species than on the SBA-type materials. The shoulders at 593 K on zirconia and 853 K on alumina can be ascribed to agglomerated O_h Mo species as inferred from the UV–vis DRS characterization.

The thermograms of NiMo precursors are given in Fig. 4. Two pronounced effects are observed after adding Ni, i.e., the shift of the first reduction peak to lower temperatures compared with the Mo counterparts and the significantly higher H_2 consumption between 573 and 773 K. These changes indicate the increase in the proportion of O_h Mo species and the promotion of the reduction of the same species. These general effects are much smaller on alumina where the second reduction peak remains as the most intense. Note that on all materials, the intensity of the reduction peaks at high temperatures decreases but their positions do not shift compared with the Mo counterparts. Hence, the proportion of Mo species that are reduced at high temperatures decreases but the reduction temperature of such species is not affected. Although the presence of T_d Mo species in the oxide precursor cannot be unambiguously asserted only on the basis of TPR results, the UV–vis spectra of the precursor and observations of tetrahedral or monomolybdate species on alumina, zirconia, or silica surfaces support our interpretations [7,43,47,48].

The H_2S profiles observed in the TPS experiments of the oxide precursors are shown in Fig. 5. In general, H_2S is consumed below temperatures about 500 K. Then, the samples release H_2S producing maxima between 500 and 570 K. Finally, continuous H_2S consumption is observed before returning to the zero line at 680 K. Only the catalysts supported on ZrO_2 exhibited a continuous H_2S consumption. According to Arnoldy and coworkers [49], the TPS process can be described as follows. The sulfidation below 500 K occurs through substitution by S of the O bound to Mo^{6+} and the reduction of these cations to Mo^{4+} through rupture of Mo–S bonds and formation of elemental S. The S deposited on the support is reduced with H_2 to H_2S at 500–570 K leading to a H_2S production signal. The H_2S consumption at temperatures above 570 K is ascribed mainly to O–S exchange on Mo^{4+}. The different steps of this sulfidation process could overlap on zirconia leading to the observed continuous H_2S consumption. Unfortunately, we were not able to determine quantitatively the H_2S consumption in the TPS experiments. However, some qualitative observations can be mentioned, e.g., the net H_2S uptake on the Mo catalyst supported on SBA-15 and ZrO_2(25)SBA was 15% and 10% higher than on Al_2O_3 or ZrO_2. It can also be safely asserted that the NiMo oxide precursors consume more H_2S than the respective Mo materials (Fig. 5). This suggests higher sulfidation degrees for the Ni-promoted catalysts than for the unpromoted catalysts. Furthermore, a significant shift of the H_2S-release peak to lower temperatures was observed on the $NiMo/Al_2O_3$ catalyst indicating that Ni has a stronger effect on the catalyst supported on alumina easing the sulfidation.

3.2. Characterization of Mo- and NiMo-sulfide catalysts

The powder XRD patterns of selected sulfided catalysts are presented in Fig. 6. The catalysts supported on ZrO_2, Al_2O_3, or ZrO_2(25)SBA did not show the presence of any Mo phase. The only present crystalline phases were those observed in the respective oxide precursors, i.e., monoclinic (JCPDS card 37-1484) and tetragonal ZrO_2 (JCPDS card 17-0923) in Mo/ZrO_2, γ-Al_2O_3 (JCPDS card 29-0063) in Mo/Al_2O_3 and tetragonal ZrO_2 in Mo/ZrO_2(25)SBA. The Mo and NiMo catalysts supported on SBA-15 exhibited diffraction peaks corresponding to MoS_2 (JCPDS card 37-1492). The intensity of these peaks was higher on the Mo/SBA-15 unpromoted catalyst pointing to higher dispersion on the promoted counterpart. The NiMo catalysts supported on others materials exhibited the same XRD patterns (not shown) observed for the corresponding Mo catalysts.

The HRTEM study was focused on catalysts supported on SBA-15, Al_2O_3, ZrO_2, and ZrO_2(25)SBA. Typical MoS_2 fringes with 6.2 Å interplanar distance were observed in all the micrographs of the sulfided catalysts. Representative micrographs of the NiMo catalyst supported on SBA-15 and ZrO_2(25)SBA are presented in Fig. 7.

The length and number of layers distributions of MoS_2 for the Mo catalysts are presented in Fig. 8. More than 50% of the observed crystals of MoS_2 have monolayers, and more than 35% have two layers on alumina or zirconia. The layer-stacking distribution is

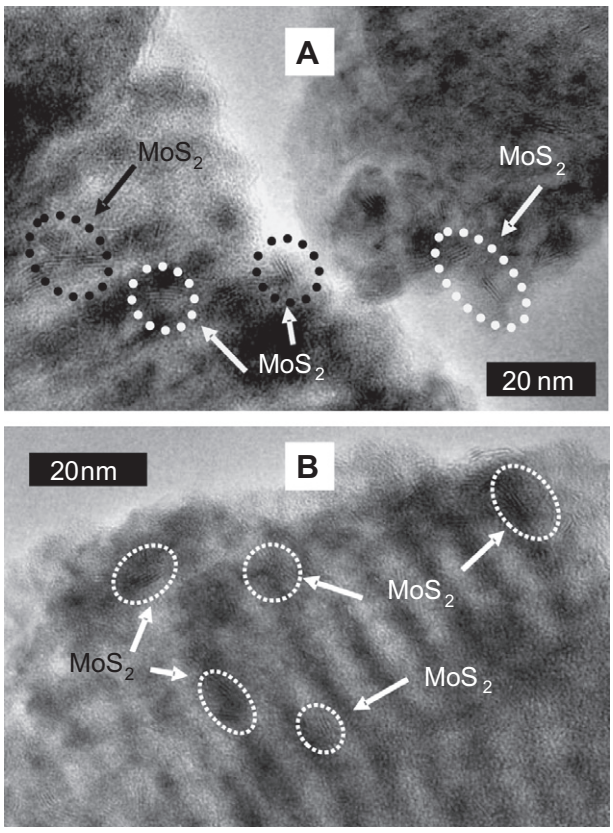

Fig. 7. Micrograph of NiMo/SBA-15 (A) and NiMo/ZrO_2(25)SBA-15 (B) catalysts. The MoS_2 particles are highlighted.

quite broad on SBA-15; for instance, 10% of the crystals have five or more layers, and the percentage of monolayers is 9%. In contrast, more than 80% of the crystals have 2 or 3 layers on ZrO_2(25)SBA. It is clear in Fig. 8-b that the length distribution is also highly homogenous on ZrO_2(25)SBA; the length of more than 60% of the MoS_2 particles is limited in the 21- to 40-Å range. Crystals longer than 60 Å are not detected on this material. The distributions are less homogeneous on pure oxides, even though most of the crystal lengths are also in the range of 21–60 Å.

The length and layer-stacking distributions of MoS_2-type structures on the NiMo catalysts preserve the trend observed for Mo catalysts as shown in Fig. 9. The presence of Ni reduces the crystal length but increases the stacking degree in the promoted catalysts compared with the corresponding Mo counterparts.

The average length and number of layers of the MoS_2 particles in each catalyst are presented in Table 2. The most stacked MoS_2 particles were obtained on pure SBA-15 (n = 2.6) among Mo catalysts. The stacking degree slightly decreased with the ZrO_2 loading to 2.3. On alumina and zirconia, the MoS_2 had the lowest stacking degree (1.4–1.5). On the other hand, the longest crystals are obtained on the pure Al_2O_3 (59 Å) followed by SBA-15 and ZrO_2 with 52 and 49 Å, respectively. The ZrO_2(25)SBA material propitiates the shorter MoS_2 particles with an average size of 36 Å. On the NiMo catalysts, the biggest crystals are formed on SBA-15 with an average size of 47 Å and 3.6 layers. The number of layers is around 2 on ZrO_2 and Al_2O_3 with crystal size of 46 and 36 Å, respectively. The MoS_2 phase supported on ZrO_2(25)SBA has the medium stacking degree of 2.9 and the shortest length (31 Å).

The average fraction of Mo atoms on the edge surface of the MoS_2 crystals denoted as "f_{Mo}" is a dispersion indicator of the active surface of the crystal [50]. The f_{Mo} value is determined from Eq. (5), assuming that the MoS_2 crystals are perfect hexagons [51]. In Eq. (5), the numerator is the number of atoms in the active surface (edges) and the denominator is the total number of Mo atoms in the crystal; "t" is the number of layers in the MoS_2 particles and "n_i" is the number of Mo atoms in one edge, determined from the length L (HRTEM) as shown in Eq. (6).

$$f_{Mo} = \frac{\sum_{i=1,\ldots,t}(6n_i - 6)}{\sum_{i=1,\ldots,t}(3n_i^2 - 3n_i + 1)} \quad (5)$$

$$n_i = \frac{L}{6.4} + 0.5 \quad (6)$$

We propose in this work a second structure factor, i.e., the average fraction of Mo atoms in the edge surface of the MoS_2 crystal out of the layer attached to the support "f'_{Mo}". The aim of this fraction is exploring the relation between the morphology of MoS_2 and the HDS of DBT-type compounds. This fraction is obtained from Eq. (7) where the denominator is the total number of Mo atoms in the crystal and the numerator is the number of atoms in the MoS_2 edges without considering one layer. Note that the difference between Eqs. (5) and (7) is the term "$t - 1$" in the numerator of Eq. (7). Aim of such modification is to obtain the average fraction of active surface that is not too close to the support, where stronger steric hindrance is expected [52].

$$F'_{Mo} = \frac{\sum_{i=1,\ldots,t-1}(6n_i - 6)}{\sum_{i=1,\ldots,t}(3n_i^2 - 3n_i + 1)} \quad (7)$$

The values for f_{Mo} and f'_{Mo} were determined using the information obtained from HRTEM (see Table 3). For the f_{Mo} values, the observed trends in terms of the support were γ-Al_2O_3 < SBA-15 < ZrO_2 < ZrO_2(25)SBA for the Mo catalysts and SBA-15 < ZrO_2 < γ-Al_2O_3 < ZrO_2(25)SBA for the NiMo catalysts. In the case of f'_{Mo} values, the

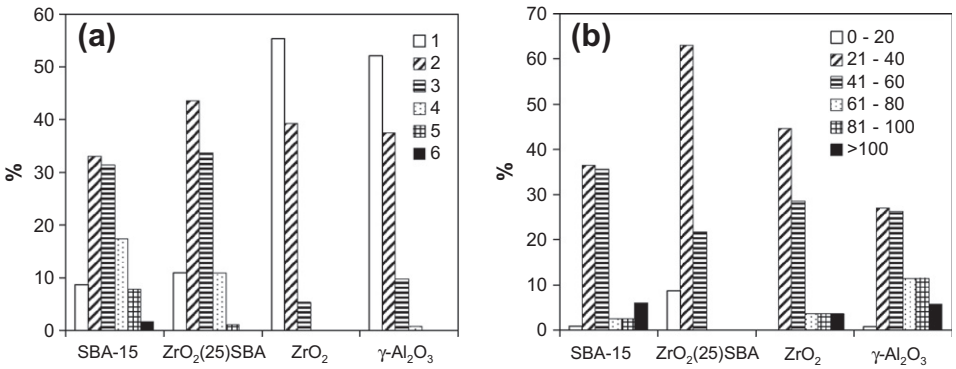

Fig. 8. Number of layers (a) and length in Å (b) of the MoS_2 particles in the Mo catalysts supported on selected materials.

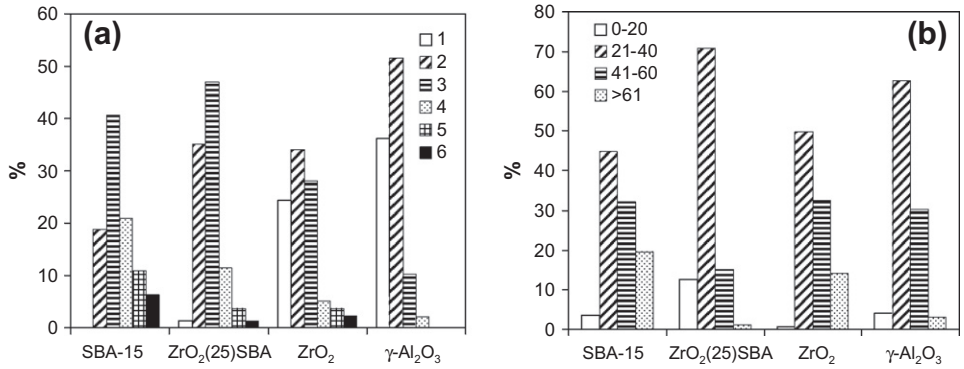

Fig. 9. Number of layers (a) and length in Å (b) of the MoS_2-like particles in the NiMo catalysts supported on selected materials.

Table 2
Average length (L) and number of layers (t) of the MoS_2 phase in Mo and NiMo catalysts supported on selected materials.

Catalyst	t	L (Å)
Mo/SBA-15	2.6	52
Mo/ZrO_2(25)SBA	2.3	36
Mo/ZrO_2	1.4	49
Mo/γ-Al_2O_3	1.5	59
NiMo/SBA-15	3.6	47
NiMo/ZrO_2(25)SBA	2.9	31
NiMo/ZrO_2	2.1	46
NiMo/γ-Al_2O_3	1.8	36

Table 3
Average fraction of Mo atoms in the edge surface of the MoS_2 crystals (f_{Mo}) and average fraction of Mo atoms in the edge surface of the MoS_2-type crystals out of the layer attached to the support (f'_{Mo}) in Mo and NiMo catalysts; concentration of adsorbed NO (μmol $g^{-1}_{catalyst}$).

Support	Mo			NiMo		
	f_{Mo}	f'_{Mo}	$NO_{ads.}$	f_{Mo}	f'_{Mo}	$NO_{ads.}$
SBA-15	0.23	0.14	160.7	0.25	0.18	170.3
ZrO_2(25)SBA	0.32	0.18	240.1	0.37	0.24	265.9
ZrO_2	0.24	0.07	175.9	0.26	0.14	190.1
γ-Al_2O_3	0.21	0.07	147.8	0.32	0.14	196.9

trends obtained for Mo and NiMo catalysts were ZrO_2(25)SBA > SBA-15 > ZrO_2 = γ-Al_2O_3. The addition of Ni had a more pronounced effect on f_{Mo} and f'_{Mo}, when added to the systems supported on alumina and zirconia. Note that the unpromoted active phase supported on alumina showed the lowest dispersion (f_{Mo}) whereas on the alumina-supported NiMo catalyst the active phase was the most dispersed among those supported on pure oxides. However, the active phase was always more disperse on the ZrO_2(25)SBA than on pure oxides. In general, Ni increases the stacking degree and shortens the length of the MoS_2 clusters (Table 2), presumably forming the NiMoS phase as discussed below. In other words, promotion increases the total dispersion of active surface f_{Mo} and the number of slabs that are not in contact with the support f'_{Mo}.

NO adsorbs on the exposed cations of promoted or unpromoted MoS_2; thus, the concentration of adsorbed NO is correlated with the edge dispersion of the catalyst [53]. It is observed in Table 3 that the total uptake of NO on the sulfide catalysts follows the same increasing trend than that observed for the f_{Mo} value, i.e., Mo/Al_2O_3 < Mo/ZrO_2 < Mo/SBA-15 < Mo/ZrO_2(25)SBA for Mo catalysts and NiMo/SBA-15 < NiMo/ZrO_2 < NiMo/Al_2O_3 < Mo/ZrO_2(25)SBA for promoted catalysts. Furthermore, the effect of the Ni promotion was stronger on alumina where the concentration of adsorbed NO increases around 33%. On the other supports, the adsorption of NO on the sample increases around 10% after Ni loading. Thus, it is confirmed that the f_{Mo} values correlate well with the dispersion of the active surface on the sulfide catalysts.

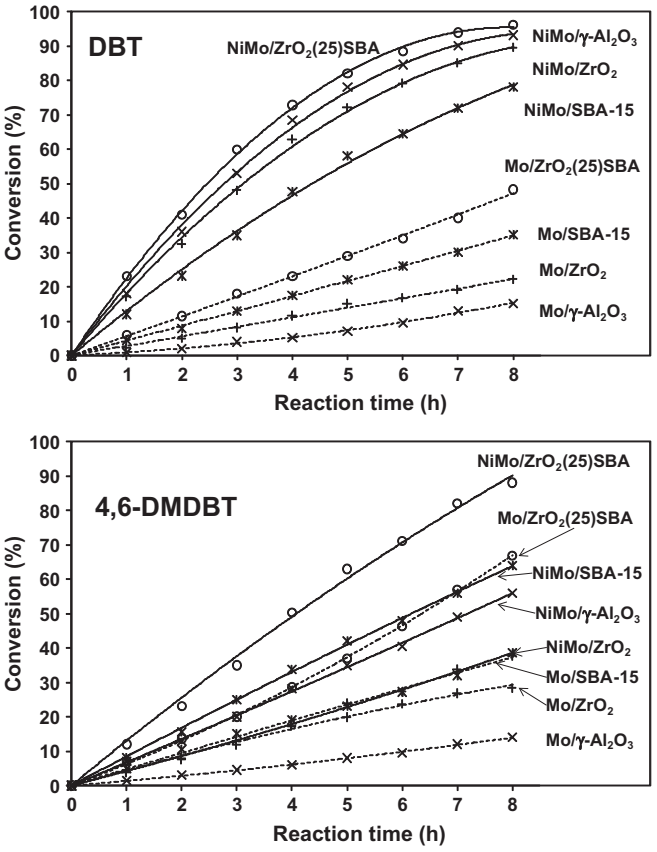

Fig. 10. Conversions of DBT and 4,6-DMDBT at different reaction times over Mo (dashed lines) and NiMo (continuous lines) catalysts supported on selected materials (573 K, 7.3 MPa H_2).

3.3. Catalytic activity

The activity of Mo and NiMo catalysts series supported on ZrO_2(x)SBA-15 and pure oxides was determined in the simultaneous HDS of DBT and 4,6-DMDBT. The conversion of both reactants is presented in Fig. 10. The results obtained over the catalysts supported on ZrO_2(25)SBA were plotted as a representative of the catalyst supported on ZrO_2-modified SBA-15. The trends

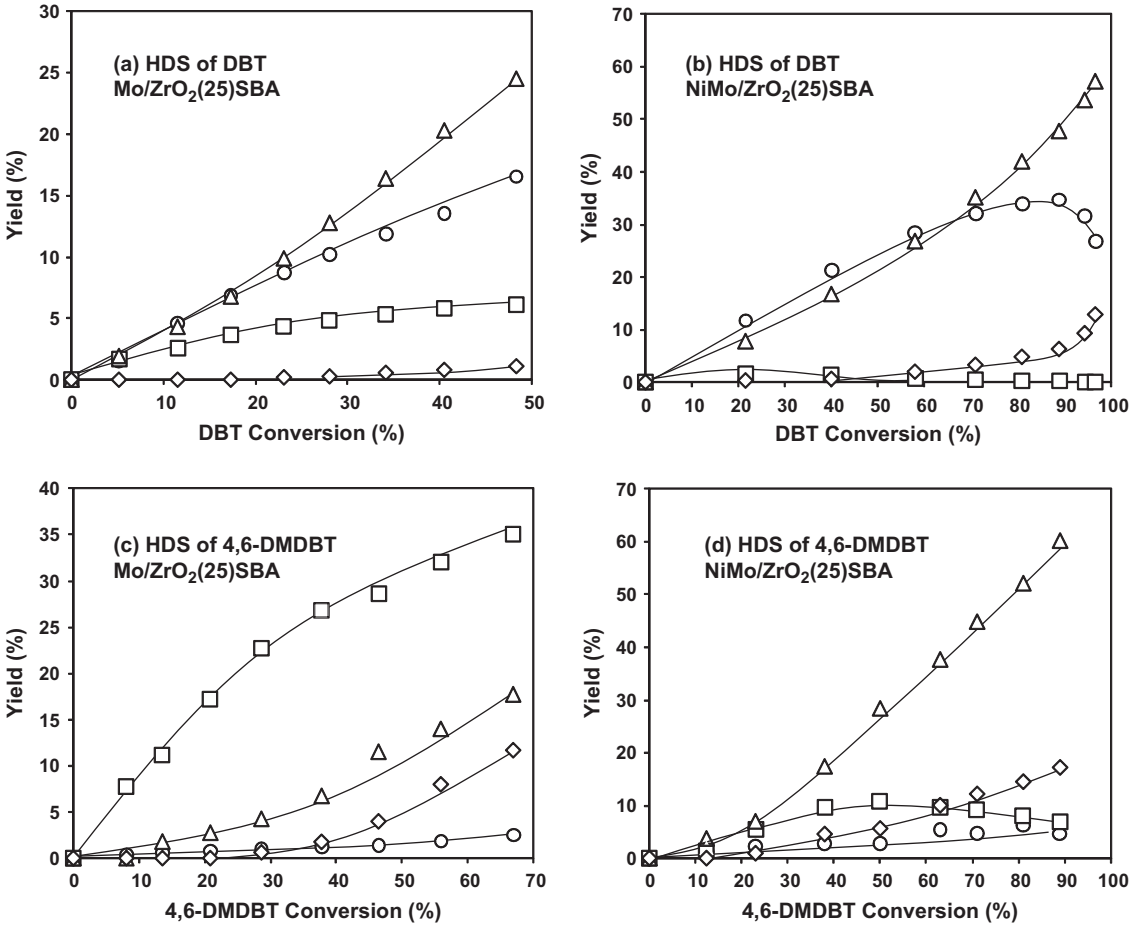

Fig. 11. Product yield along with the conversion from the HDS of DBT (a and b) and 4,6-DMDBT (c and d) detected on $Mo/ZrO_2(25)SBA$ (a and c) and $NiMo/ZrO_2(25)SBA$ (b and d). In (a and b): tetrahydrodibenzothiophene (□), biphenyl (○), cyclohexylbenzene (Δ), and dicyclohexyl (◇). In (c and d): tetrahydrodimethyldibenzothiophene and hexahydrodimethyldibenzothiophene (□), dimethylbiphenyl (○), methylcyclohexyltoluene (Δ) and dimethyldicyclohexyl (◇).

depended on the support and promotion. The addition of Ni increased the conversion of DBT and 4,6-DMDBT on all the catalysts; supporting the catalyst on $ZrO_2(x)$SBA, however, led to the most active formulations. The conversion of both reactants over Mo catalysts followed the same increasing trend: $Mo/\gamma\text{-}Al_2O_3$ < Mo/ZrO_2 < Mo/SBA-15 < $Mo/ZrO_2(25)$SBA. The conversion of DBT on the NiMo catalysts increased in the order: NiMo/SBA-15 < $NiMo/ZrO_2$ < $NiMo/\gamma\text{-}Al_2O_3$ < $NiMo/ZrO_2(25)$SBA. The conversion of 4,6-DMDBT on NiMo catalysts increased as follows: $NiMo/ZrO_2$ < $NiMo/\gamma\text{-}Al_2O_3$ < NiMo/SBA-15 < $NiMo/ZrO_2(25)$SBA.

The main detected products in the HDS of DBT were tetrahydrodibenzothiophene (THDBT), biphenyl (BP), cyclohexylbenzene (CHB), and dicyclohexyl (DCH). The products from the HDS of 4,6-DMDBT were tetrahydrodimethyldibenzothiophene (THDMDBT), hexahydrodimethyldibenzothiophene (HHDMDBT), dimethylbiphenyl (DMBP), methylcyclohexyltoluene (MCHT), and dimethyldicyclohexyl (DMDCH). Only at DBT and 4,6-DMDBT conversion above 70% on the NiMo catalysts, small amounts of benzene, toluene, cyclohexane and methylcyclohexane were detected. The small concentration of those products and the absence of isomers of 4,6-DMDBT indicated a very low acidity of the materials here were studied. On the contrary, high concentration of isomers and products from C–C bond cleavage reactions has been observed on Al^{3+}-modified SBA-15 due to the contribution of acid sites in the silica support doped with trivalent ions [24].

For the sake of brevity, only the product distributions observed on (Ni)Mo/Zr(25)SBA are presented here (Fig. 11), the activity results obtained on the other systems are described below as pseudo-first-order constants. Some general comments apply for all the systems. As described in Fig. 1, the hydrogenated dibenzothiophenic and the biphenylic compounds are primary products, whereas the cyclohexylbenzene- and dicyclohexyl-type compounds are secondary products. The yield of BP and CHB is similar at low DBT conversion on the Mo and NiMo catalysts; the yield of DMBP, however, remains very low on both catalysts at any 4,6-DMDBT conversion. The presence of Ni promotes the conversion of the hydrogenated intermediates whose yield increases steadily on Mo catalysts. Indeed, THDMDBT and HHDMDBT (lumped together in Fig. 11) are by far the most abundant products in the HDS of 4,6-DMDBT on Mo catalysts. The concentration of the fully hydrogenated and desulfurized compounds, DCH and DMDCH, is significant only at conversions above 35%; thus, the pseudo-first-order constants determined from Eqs. (1)–(4) are valid to discuss the main steps in the reaction pathway of DBT and 4,6-DMDBT.

Further description of the activity results is based on the first-order constants of the main reaction steps (Tables 4 and 5). The sum of the individual rate constants of each reaction pathway ($k_{HYD} + k_{DDS}$) is the overall rate constant, i.e., the net consumption rate of DBT or 4,6-DMDBT. It is observed that the overall reaction rate constants followed the trends above described in terms of conversion for Mo and NiMo catalysts. Furthermore, the activities of the NiMo catalyst for both reactants increased with the ZrO_2 loading in the SBA-15 up to 37 wt.% of ZrO_2 and decreased with 50 wt.% of ZrO_2 in the support.

Table 4
Pseudo-first-order constants (L(s $g_{catalyst}$)$^{-1}$ × 10^{-6}) for the main reaction steps of the HDS of DBT and 4,6-DMDBT over Mo catalysts supported on selected materials.

Support	Reactant	k_{DDS}	k_{HYD}	k_{DS}	k_{DDS} + k_{HYD}	k_{DDS}/k_{HYD}
SBA-15	DBT	1.6	2.2	12	3.8	0.7
	4,6-DMDBT	0.2	3.7	10.2	3.9	0.06
ZrO_2(25)SBA	DBT	2.9	2.3	10	5.2	1.3
	4,6-DMDBT	0.2	6.9	8.0	7.1	0.03
ZrO_2	DBT	1.7	0.5	17	2.2	3.4
	4,6-DMDBT	0.2	3.1	4.7	3.3	0.06
γ-Al_2O_3	DBT	0.9	0.3	14	1.2	3
	4,6-DMDBT	0.1	1.1	2.4	1.2	0.01

Table 5
Pseudo-first-order constants (L(s $g_{catalyst}$)$^{-1}$ × 10^{-6}) for the main reaction steps of the HDS of DBT and 4,6-DMDBT over NiMo catalysts supported on selected materials.

Support	Reactant	k_{DDS}	k_{HYD}	k_{DS}	k_{DDS} + k_{HYD}	k_{DDS}/k_{HYD}
SBA-15	DBT	5.1	6.9	256	11.9	0.74
	4,6-DMDBT	0.73	6.8	71	7.6	0.1
ZrO_2(25)SBA	DBT	10.1	9.4	387	19.5	1.1
	4,6-DMDBT	0.88	13.7	133	14.6	0.06
ZrO_2(37)SBA	DBT	11.3	10.2	477	21.5	1.1
	4,6-DMDBT	0.98	16.4	159	17.3	0.06
ZrO_2(50)SBA	DBT	10.6	8.7	342	19.3	1.2
	4,6-DMDBT	1.3	14.3	102	15.6	0.09
ZrO_2	DBT	12.3	4.6	440	16.5	2.7
	4,6-DMDBT	0.35	3.6	131	3.9	0.1
γ-Al_2O_3	DBT	11.4	5.1	246	16.8	2.2
	4,6-DMDBT	0.54	5.9	136	6.4	0.1

The k_{DDS}/k_{HYD} ratio is presented in Tables 4 and 5 as an indicator of the preferred desulfurization route. The 4,6-DMDBT followed preferentially the hydrogenation pathway ($k_{DDS}/k_{HYD} < 1$), regardless of the support and the presence of promoter. The preferred route for the DBT was strongly dependent on the support. The direct desulfurization was clearly followed on zirconia and alumina ($k_{DDS}/k_{HYD} \geqslant 3$ for Mo catalysts) although the addition of Ni seems to promote the HYD pathway to the larger extent (k_{DDS}/k_{HYD} decreased to an average of 2.5). On pure SBA-15, the hydrogenation of DBT was favored over the direct sulfur removal (k_{DDS}/k_{HYD} is 0.7 and 0.74 on Mo and NiMo catalysts, respectively). The Mo catalysts supported on ZrO_2(*x*)SBA showed the k_{DDS}/k_{HYD} ratio of 1.3; thus, the DDS pathway was only slightly preferred. On NiMo catalysts supported on ZrO_2(*x*)SBA-15, the k_{DDS}/k_{HYD} ratio slightly decreased to around 1.1.

The rate constant k_{DS} shows the ability of the catalyst to remove the sulfur from the hydrogenated intermediates. The values indicate that the hydrogenated intermediates are more reactive than the starting DBT-type compounds. The k_{DS} values are one order of magnitude higher than the k_{DDS} values for the same reactant on Mo catalysts. The promotion with Ni had a dramatic effect on the desulfurization of hydrogenated intermediates as the values of k_{DS} for both molecules over NiMo catalysts (Table 5) are two or three orders of magnitude higher than the values observed using the corresponding Mo catalysts (Table 4).

These results were in accordance with previous reports where the activity of promoted and unpromoted Mo catalysts supported on ZrO_2-modified SBA-15 were higher than the counterparts supported on other materials for the HDS of DBT and 4,6-DMDBT in separate reaction steps [23,25–27,40–42]. In Table 6, the pseudo-first-order constants for selected catalysts determined here are compared with the constants determined in the HDS of the single model compounds as determined in previous studies. Clearly, the values for a given compound and catalytic system are very similar; in the cases that the reaction constants differ significantly, trends are not observed. Thus, the apparent variations in the pseudo-first-order constant can be attributed to the slight differences between the catalysts used in the different studies. The similarity between reaction rate constants determined in the single and simultaneous HDS indicates that the effect of competitive adsorption is negligible for the determination of kinetic parameters.

4. Discussion

4.1. Effect of the oxide precursor on the sulfide catalysts

Qualitative relations between the oxide precursors and the corresponding sulfide catalysts can be stated from our results. T_d and O_h Mo species were observed on the siliceous SBA-15, the later being the most abundant species; indeed, a fraction of O_h Mo species was agglomerated to MoO_3 (XRD). In line with this heterogeneous distribution of oxide species, the sulfide catalyst supported on SBA-15 exhibited some monolayers of MoS_2 as well as the longest and most stacked MoS_2 crystals. Some MoS_2 particles on SBA-15 were large enough to be detected by XRD. The major proportion of T_d Mo species on alumina and zirconia led mainly to MoS_2 monolayers in the sulfided catalysts. The predominance of O_h Mo species on ZrO_2(*x*)SBA with high dispersion led to MoS_2 clusters with medium stacking degree (2–3 layers) and short length. The higher proportion of O_h Mo species led to MoS_2 crystals with more layers on the NiMo catalysts than on the unpromoted counterparts.

The relation between oxide precursors and Mo catalysts is explained in terms of the strength of interaction. On ZrO_2 and Al_2O_3, that have strong interactions with Mo species, the reduction of an important fraction of Mo species is possible only at high temperature, i.e., the T_d Mo species are reduced above 870 K (Fig. 4). The low reducibility points to low sulfidation degree as confirmed by the larger H_2S consumption of the oxide precursors supported on SBA-15 materials than those on Al_2O_3 or ZrO_2. Thus, not all

Table 6
Overall pseudo-first-order constants (L(s $g_{catalyst}$)$^{-1}$ × 10^{-6}) calculated on selected catalysts for the HDS of a single model molecule and the simultaneous HDS as determined in this work.[a]

	DBT		4,6-DMDBT			
Catalyst →	NiMo		Mo		NiMo	
Support ↓	Ref. [27]	This study	Ref. [41]	This study	Ref. [42]	This study
SBA-15	11.4[b]	11.9	2.9[b]	3.9	5	7.6
ZrO_2–SBA-15[c]	21.4[b]	19.5	9.2[b]	7.1	15	14.6
γ-Al_2O_3	12.5[b]	16.8	-	1.2	5.2	5.2

[a] The metal loading and the reaction conditions (573 K and 7.3 MPa H_2 pressure) are the same in all cases.
[b] Calculated from the corresponding conversion–time plots reported in the reference.
[c] The preparation procedure of this material differs; however, the ZrO_2 loading in the SBA-15 is around 23 wt.%.

Mo is bonded with S, and O linkages between MoS_2 clusters and the support exist after the sulfidation process. Conversely, on SBA-15, the weak interaction of pure silica with Mo oxide allows the development and agglomeration of O_h Mo species. The nature of this interaction propitiates multilayered MoS_2 structures after sulfidation, whereas incompletely sulfided MoS_2 clusters typically have a monolayer structure [54,55]. The medium interaction strength led to O_h Mo species that do not agglomerate on ZrO_2(25)SBA; thus, after sulfidation, the sulfide species are organized in dispersed MoS_2 slabs that do not have tendency to form monolayers.

The addition of Ni weakens the interaction of Mo species with the support (the proportion of O_h Mo species increases) and eases its reduction and sulfidation (TPR and TPS). In line with this reasoning, the effect of promotion is higher on the active sulfide phase supported on Al_2O_3 and ZrO_2, where the interaction is stronger than on SBA-type materials. Table 3 shows that f_{Mo} increases 52–58% and f'_{Mo} increases 100% after the promotion on alumina or zirconia. In contrast, the increments of f_{Mo} and f'_{Mo} are 15% and 33% on ZrO_2(x)SBA, whereas on pure SBA-15, they are only 8% and 28%, respectively. The increase in adsorbed NO after Ni promotion was also the highest on Al_2O_3.

4.2. Effect of the morphology of MoS_2 and NiMoS phases on the catalytic activity

At this point, it is stated that the physical implication of the Ni promotion is the appearance of the NiMoS phase where promoter atoms replace Mo at positions in the edges of the MoS_2 cluster according to the "Co–Mo–S" model [53]. The NiMoS phase is claimed to be intrinsically much more active that the pure MoS_2 phase mainly because of the enhancing of the activation of H_2 [56]. Although the NiMoS phase cannot be distinguished from pure MoS_2 in the micrographs or XRD patterns, the much higher intrinsic activity of the NiMo catalysts allows us to assume that the MoS_2-like structures observed in the HRTEM images correspond mainly to the NiMoS phase. Furthermore, the presence of NiS_x, expected when the Ni is not completely incorporated in the NiMoS phase [57], was neither observed by XRD nor HRTEM.

The values of f_{Mo} and f'_{Mo} were compared with the activity of Mo and NiMo catalysts. In Fig. 12, the values of the overall rate constants for the HDS of DBT and 4,6-DMDBT (denoted as k_{DBT} and $k_{4,6\text{-DMDBT}}$) on Mo catalysts were plotted against the f_{Mo} and f'_{Mo} values. The plot corresponding to the HDS on NiMo catalysts is presented in Fig. 13.

Fig. 12 shows the expected general trend of higher HDS activity at increasing f or f'_{Mo} values. However, the black symbols, corresponding to the reaction constants of both compounds correlated with the f'_{Mo} numbers, exhibit the most proportional behavior, i.e., increasing f'_{Mo} values lead always to higher rate constants. With the assumption that the f'_{Mo} values reflect the proportion of Mo atoms on the edges of MoS_2-type structures out of the bottom layer, the most feasible correlation in the case of Mo catalysts between k_{DBT}, $k_{4,6\text{-DMDBT}}$ and f'_{Mo} values suggests a very low activity of monolayers. Our discussion on the transition from Mo oxide precursors to unpromoted catalysts implies that the monolayers in these catalysts are only partially sulfided and have poor HDS activity. Thus, it is likely that most of the catalytic activity is due to MoS_2 with more than one layer where less O-bonded Mo is expected. The incomplete sulfidation of Mo species on unpromoted catalysts could also led to unclear correlations between morphology of the active phase and the catalytic performance.

Fig. 13 shows a linear correlation between f_{Mo} and the activity for the HDS of DBT as well as between f'_{Mo} and the HDS activity of 4,6-DMDBT. This linear trend clearly shows that the activity of the NiMo catalyst for the HDS of DBT depends on the dispersion of the active phase (f_{Mo}). Hence, MoS_2 monolayers in the NiMo catalyst are active in the HDS of DBT as well as stacks of MoS_2 in agreement with the literature [58]. The MoS_2 stacks in the NiMo catalyst can be easily assigned to the NiMoS phase type II that tends to form stacked structures with sparse oxygen. It can also be assumed that the monolayers in the NiMo catalysts correspond to type II NiMoS monolayers with minimal interaction with the support and high activity in the HDS of not-hindered DBT-type compounds [57]. Interestingly, the activity of the promoted catalysts in the HDS of 4,6-DMDBT correlates with the f'_{Mo} values (fraction of edges that are not deposited directly on the supports). Consequently, the monolayers of MoS_2-type structures and the slab that is attached to the support in a stack have limited or no interaction with 4,6-DMDBT regardless the sulfidation degree.

A qualitative relation arises between f'_{Mo} for Mo and NiMo catalysts and the reaction rate constant of the hydrogenation route (k_{HYD}). The value of f'_{Mo} increases, depending on the support, in the order Al_2O_3 < ZrO_2 < SBA-15 < ZrO_2(x)SBA. The values of k_{HYD} for DBT and 4,6-DMDBT follow the same trend. This is well in line

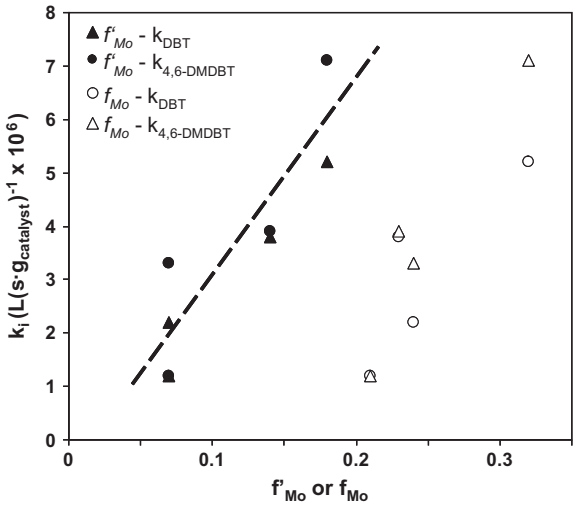

Fig. 12. Overall reaction rate constants of the HDS of DBT and 4,6-DMDBT on Mo catalysts correlated with the f_{Mo} and f'_{Mo} values.

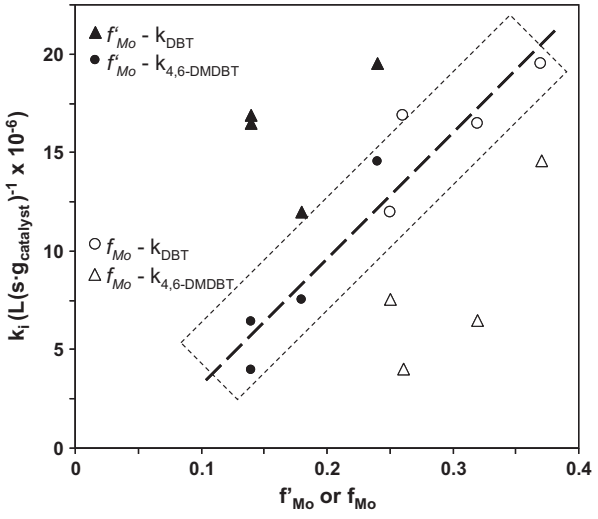

Fig. 13. Overall reaction rate constants of the HDS of DBT and 4,6-DMDBT on NiMo catalysts correlated with the f_{Mo} and f'_{Mo} values.

with previous observations that the hydrogenation ability of the catalyst is favored by multilayered MoS_2 clusters [23,49,59].

The formation of NiMoS does change not only the morphology but also the intrinsic activity of the MoS_2-like phase. This is evident in the dramatic increase in the rate constant of desulfurization of hydrogenated intermediates (k_{DS}) after Ni promotion, which cannot be explained by the changes in MoS_2 morphology. It seems that the NiMoS phase fastens the regeneration of active sites or creates new centers especially active for sulfur removal from hydrogenated intermediates. This is well in line with other reports that claim that the promoter enhances the rate of C–S bond breaking [33]. As a consequence of this "electronic" influence of Ni, the results from Mo and NiMo catalysts (Figs. 12 and 13) cannot be compared in terms of morphology of the active phase.

The above discussed correlations between the structure factors (f_{Mo} and f'_{Mo}) and the activity suggest that any possible influence of the support during reaction has a minor importance in the HDS process. The effect of the studied supports on the HDS of DBT-type compounds seems to be limited to the relation between interaction strength and MoS_2 or NiMoS morphology. Thus, it is worthing to emphasize the characteristics of the active phase in the (Ni)Mo/ZrO_2(x)SBA catalysts. The length and layer-stacking degree of the MoS_2-type particles are very homogenous on ZrO_2(25)SBA (Figs. 8 and 9). Most of the clusters have relatively narrow range of length, whereas between 70% and 80% of MoS_2 crystals were composed by two or three layers. This average characteristics of the active phase on ZrO_2(x)SBA would lead to the morphology that maximizes the amount of accessible active sites. Low deactivation has been observed in long-term reactions in trickle bed reactor using SBA-15-supported HDS catalysts [60,61]. Thus, the NiMo/ZrO_2–SBA-15 system is a good candidate to be scaled up; however, this issue depends on many other factors that are not in the scope of this study.

Fig. 14 shows an schematic representation of the interaction of DBT and 4,6-DMDBT with the supported Mo and NiMo catalysts. From our results, we conclude that pure MoS_2 is present in the former case, whereas NiMoS is the representative phase in the promoted catalysts. Note that both phases show the same structure in HRTEM. The morphology–activity relations for unpromoted catalysts suggest that the MoS_2 layer attached to the support has low reactivity in the HDS of both molecules. This is possibly due to the presence of oxygen bonds to the support that lessen the activity of the slabs. The formation of the NiMoS phase on the promoted catalysts decreases the interaction with the support and maximizes the activity and accessibility of the active surface. All the slabs are accessible for DBT while 4,6-DMDBT has restricted interaction with the slab adjacent to the support because of steric hindrance. The selectivity is ruled in first instance by the morphology of the dibenzothiophenic compound and in a minor extent in the stacking degree. This is that hydrogenation is always the preferred pathway in the HDS of 4,6-DMDBT, whereas DBT reacts by DDS or HYD without any intrinsic preference. On highly stacked MoS_2-like clusters, however, the HYD activity of the catalysts increases. The subsequent removal of sulfur from the hydrogenated intermediates, e.g., HHDMDBT to DMDCH in Fig. 14, is considerably faster on the promoted phase than on the MoS_2.

4.3. On the active sites in the MoS_2 and NiMoS phases

The nature of the active sites in MoS_2 or NiMoS is still controversial. It is accepted that coordinatively unsaturated sites located on the edge of the MoS_2 slabs are the active sites for hydrogenolysis reactions [33]. Adsorption and hydrogenation of aromatic rings have been attributed to adjacent unsaturated Mo atoms with specific chemical environment [33], whereas the adsorption and hydrogenation of thiophenic rings have been claimed to occur on the fully sulfide edges of MoS_2 that exhibit metallic characters (brim sites) [62]. All postulated theories imply, however, that the active phase of the HDS catalyst has two kinds of active sites for the HDS of DBT-type compounds; one catalyzes the direct removal of S (hydrogenolysis site) and the other is active for hydrogenation steps. The performance of the catalyst is determined by the balance between hydrogenation and desulfurization sites. Note that the values of the reaction rate constants determined in this work are proportional to the concentration of active sites because the concentration of products and reactants adsorbed on the surface can be considered constant at low conversions for all the experiments. Thus, the rate constants can be used to discuss the catalytic performance in terms of concentration of active sites.

The reaction rates of the HDS of 4,6-DMDBT are comparable with those of DBT on Mo catalysts, which indicates that 4,6-DMDBT is not intrinsically less reactive. The hydrogenation of 4,6-DMDBT is ten times faster than its direct desulfurization whereas the k_{DDS}/k_{HYD} ratio for the HDS of DBT is close to one on SBA-type materials and around 2 on zirconia and alumina. This clear difference in the preferred reaction pathway for each reactant is not dependent on the promotion in a large extent. Thus, we infer that the difference in selectivity depends more on the geometry of adsorption of the reactant on the active sites than on the morphology of the active phase. A flat adsorption mode (the aromatic rings approach parallel to the surface) is required to hydrogenate the reactant molecule either on the vacancies [63] or on brim sites [62,64] whereas a perpendicular absorption via S-metal bonding leads to hydrogenolysis [65]. The methyl groups in the 4 and 6 positions in 4,6-DMDBT do not inhibit the flat adsorption mode but they hamper the perpendicular adsorption [66]. It is likely that both kinds of active sites are accessible for DBT but 4,6-DMDBT reacts mainly on hydrogenation sites.

With the aim of clarifying the discussion, the k_{DDS}/k_{HYD} ratio (Tables 4 and 5) of the HDS of DBT and 4,6-DMDBT on Mo and NiMo catalysts are plotted in Fig. 15. Regardless of the promoter, the ratios are around 1 for the HDS of DBT on Mo and NiMo catalyst supported on SBA-type materials. Under the assumption that DBT reacts on both kinds of sites, the ratio close to 1 suggests a balanced proportion of sites. Conversely, the k_{DDS}/k_{HYD} ratio is clearly

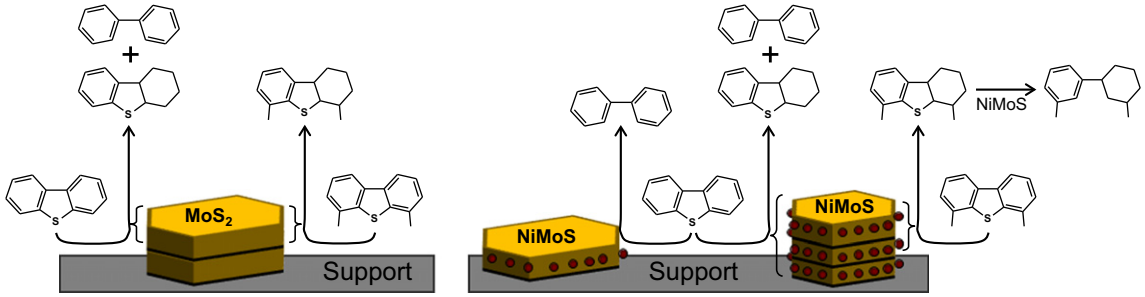

Fig. 14. Schematic representation of the interaction of DBT and 4,6-DMDBT with supported MoS_2 and NiMoS phase.

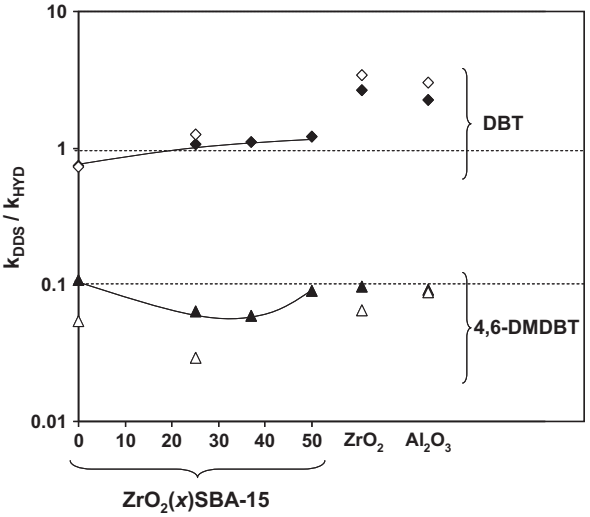

Fig. 15. k_{DDS}/k_{HYD} observed in the HDS of DBT and 4,6-DMDBT over Mo (white symbols) and NiMo (black symbols) catalysts supported on the materials shown in the *x* axis.

higher than 1 on Al_2O_3 and ZrO_2, confirming the general agreement that desulfurization sites are much more abundant than hydrogenation sites on alumina and zirconia. The k_{DDS}/k_{HYD} ratio for the HDS of 4,6-DMDBT below 0.1 reflects the difficulty of this molecule to adsorb on desulfurization sites. Note in Fig. 15 that the k_{DDS}/k_{HYD} ratio for the HDS of 4,6-DMDBT is higher on promoted catalysts than on Mo catalysts. This points to the enhancement of direct desulfurization sites or the creation of new active sites in the NiMoS phase that are able to directly desulfurize the 4,6-DMDBT after promotion, which are related to the dramatic enhancement of sulfur removal from hydrogenated intermediates (k_{DS}).

The morphology of MoS_2 phase has been quantitatively related to the overall HDS activity of DBT and 4,6-DMDBT. It is also noticed that the multilayered structures favor the hydrogenation pathway of both molecules. The k_{DDS}/k_{HYD} ratio, however, cannot be correlated with f_{Mo} or f'_{Mo}. This indicates that the hydrogenolysis activity is not determined by the number of layers of the MoS_2 crystal. Furthermore, the hydrogenation activity depends on the structure but the hydrogenation sites are not limited to the "top" slabs as the adsorption on "brim sites" implies. It is clear that less stacked clusters of MoS_2 should have higher proportion of "top" slabs, i.e., the monolayers of MoS_2 or NiMoS should have high hydrogenation ability because the flat adsorption on the basal plane is not constrained. This is contrary to our results and to the behavior generally accepted of MoS_2 monolayers. Thus, the adsorption and subsequent hydrogenolysis or hydrogenation of DBT-type compounds can be ascribed to coordinatively unsaturated sites at the perimeter of the (1 0 1 0) plane in all the MoS_2 slabs. The planar adsorption of a DBT molecule would require an approximate area of 9.5 × 5 Å, whereas the distance of an exposed Mo cation in the first slab to the support should be smaller than 6.1 Å (the distance between Mo atom layers in two stacked MoS_2 slabs). Thus, the flat absorption of DBT or 4,6-DMDBT on active sites located on the (1 0 1 0) planes would strongly be affected by the support. For stacked MoS_2 particles, the increasing distance to the support leads more space to the reactants for the adsorption required for hydrogenation. The metal–sulfur perpendicular adsorption is possible on monolayers because the molecule adsorbs perpendicularly to the active phase, parallel to the support.

It is possible to determine turnover frequency (TOF) values by dividing the pseudo-first-order constants by either the overall dispersion given by f_{Mo} or the concentration of NO adsorbed in the sample (other parameters must be included to obtain units of frequency). Understanding the physical meaning of those TOF values, however, is not straightforward because not all the active sites would be accessible for the dibenzothiophenic compounds, specially for 4,6-DMDBT. Furthermore, calculating TOF values for each pathway is not possible because the fraction of active surface (or active sites) where HYD and DDS occur remains unknown. The calculation of TOF values for each pathway from the same dispersion parameter (NO adsorbed or structure factor) would lead to artifacts, e.g., the HYD sites are much more active to convert 4,6-DMDBT than DBT. In contrast, evaluating overall values of TOF from ($k_{DDS} + k_{HYD}$) is important to evidence the structure–activity correlations proposed in this study.

Table 7
Turnover frequency values (h^{-1}) on Mo and NiMo catalysts determined from the overall pseudo-first-order constants and the corresponding f_{Mo} and f'_{Mo} values. Turnover frequency values ($s^{-1}\,mol^{-1}$) determined from the overall pseudo-first-order constants and the corresponding concentration of adsorbed NO.

Support	Reactant	Mo			NiMo		
		f_{Mo}	f'_{Mo}	$NO_{ads.}$	f_{Mo}	f'_{Mo}	$NO_{ads.}$
SBA-15	DBT	0.22	0.37	0.59	**0.65**	0.9	***1.76***
	4,6-DMDBT	0.23	0.38	0.61	0.41	**0.58**	1.11
Zr(25)SBA	DBT	0.22	0.39	0.54	**0.71**	1.1	***1.83***
	4,6-DMDBT	0.3	0.51	0.74	0.53	**0.82**	1.37
ZrO_2	DBT	0.12	0.42	0.31	**0.86**	1.63	***2.22***
	4,6-DMDBT	0.19	0.62	0.47	0.21	**0.4**	0.52
γ-Al_2O_3	DBT	0.08	0.23	0.2	**0.7**	1.59	***2.09***
	4,6-DMDBT	0.08	0.23	0.2	0.27	**0.62**	0.82

The TOF values determined from both structure factors (f_{Mo} and f'_{Mo}) as well as from the concentration of adsorbed NO for Mo and NiMo catalysts are presented in Table 7. Clear discussion cannot be made from the TOF values of the unpromoted catalysts probably because of the not fully sulfidation of the MoS_2 phase, which is more aggravating on alumina. However, it is important to note that the TOF values on SBA-type materials are very similar, which suggest that the improving of the activity of the catalysts is not due a higher intrinsic activity of the active sites.

The case of TOF values on NiMo is much more conclusive. There is not trend among the values determined from any parameter. However, comparing the values for DBT calculated from f_{Mo} with the 4,6-DMDBT TOF values determined from f'_{Mo} (bold numbers in Table 7), it is clear that they do not differ significantly. Furthermore, the TOF values of the HDS of DBT as determined from the concentration of adsorbed NO are quite similar as well (italic bold numbers in Table 7). This has two main implications: (i) the above-mentioned assignments of active sites, i.e., all sites are accessible for DBT but only a fraction for 4,6-DMDBT, is correct; (ii) the intrinsic activity of the active sites do not depend on the support or on the structure of the molecule in a large extent. The rest of the TOF values of the NiMo catalysts (not highlighted in Table 7) are too high or too low because the fraction of accessible active sites is underestimated for DBT and overestimated for 4,6-DMDBT.

The average TOF values on Mo catalysts determined from f'_{Mo} is 0.35 and 0.44 h^{-1} for DBT and 4,6-DMDBT. The average TOF values on NiMo catalysts increase to 0.74 h^{-1} for DBT (from f_{Mo}) and 0.6 h^{-1} for 4,6-DMDBT (from f'_{Mo}). On the other hand, the TOF values determined from the adsorption of NO increase up to ten times after the addition of Ni. These variations substantiate the promoter effect of Ni, i.e., the higher HDS performance of the NiMoS phase than that of the pure MoS_2.

5. Conclusions

According to the above-mentioned results, the following conclusions can be stated.

The characteristics of the oxide Mo species depend on the interaction strength with the support. The increasing proportion of T_d Mo species indicates stronger interactions. The highest proportion of O_h Mo species with the maximum dispersion was found among the studied catalysts on $ZrO_2(x)$SBA supports.

The characteristics of the oxide species on $ZrO_2(x)$SBA conduct to MoS_2 clusters with short length (36 and 31 Å on Mo and NiMo catalysts respectively) and 2–3 layers in average. Such morphology maximizes the active surface and the proportion of slabs sterically unhindered for the proximity of the support. Consequently, the catalytic system NiMo/$ZrO_2(x)$SBA-15 is an outstanding catalyst because it can convert and extract sulfur from two kinds of DBT-type compounds with different behaviors in HDS.

It is shown that the intrinsic HDS activity of the catalysts does not depend importantly on the composition of the support. In contrast, the formation of the NiMoS phase and the morphology of the active phase are the key factors in the HDS of DBT-type compounds.

The MoS_2 monolayers in unpromoted catalysts have low activity in the HDS of both DBT-type compounds. In promoted catalysts (NiMoS phase), the sulfide monolayers or the layer attached to the support in a multilayered cluster is active for the HDS of DBT, but has little activity for the HDS of 4,6-DMDBT. This is not related to a different location of hydrogenation and hydrogenolysis sites in the MoS_2 cluster but to the structure of the reactant molecule and the space available for the interaction with the active sites. In the proximity of the support, the flat adsorption is hindered and thus, 4,6-DMDBT that adsorbs preferably in this mode does not react on sulfide monolayers.

Acknowledgments

Financial support by CONACYT-Mexico (Grant 100945) is gratefully acknowledged. The authors thank M. Aguilar Franco, C. Salcedo Luna and I. Puente Lee and for their technical assistance with XRD and HRTEM characterizations. The authors also thank Professor J.A. Lercher for providing laboratory facilities for the characterization of sulfided materials at the Catalysis Research Center in the Technische Universität München.

References

[1] C. Hsu, P. Robinson, Practical Advances in Petroleum Processing, Springer, USA, 2006. p. 866.
[2] A. Ishihara, F. Dumeignil, J. Lee, K. Mitsuhashi, E. Qian, T. Kabe, Appl. Catal. A 289 (2005) 163.
[3] F. Dumeignil, K. Sato, M. Imamura, N. Matsubayashi, E. Payen, H. Shimada, Appl. Catal. 315 (2006) 18.
[4] M. Nagai, T. Fukiage, S. Kurata, Catal. Today 106 (2005) 201.
[5] E. Kraleva, A. Spojakina, K. Jiratova, L. Petrov, Catal. Lett. 112 (2006) 203.
[6] H. Shimada, T. Sato, Y. Yoshimura, J. Hiraishi, A. Nishijima, J. Catal. 110 (1988) 275.
[7] M. Jia, P. Afanasiev, M. Vrinat, Appl. Catal. A 278 (2005) 213.
[8] M. Jia, P. Afanasiev, M. Vrinat, W. Li, H. Xu, Q. Ge, Petrochem. Technol. 33 (2004) 202.
[9] J. Weissman, E. DeCanio, J. Edwards, Catal. Lett. 24 (1994) 113.
[10] S. Damyanova, L. Petrov, P. Grange, Appl. Catal. A 239 (2003) 241.
[11] M. Rana, S. Maity, J. Ancheyta, G. Murali Dhar, T. Prasada Rao, Appl. Catal. A 268 (2004) 89.
[12] M. Barrera, M. Viniegra, J. Escobar, M. Vrinat, J. de los Reyes, F. Murrieta, J. García, Catal. Today 98 (2004) 131.
[13] J. Lee, S. Han, H. Kim, J. Koh, T. Hyeon, S. Moon, Catal. Today 86 (2003) 141.
[14] A. Wang, Y. Wang, T. Kabe, Y. Chen, A. Ishihara, W. Qian, J. Catal. 199 (2001) 19.
[15] T. Klimova, M. Calderón, J. Ramírez, Appl. Catal. A 240 (2003) 29.
[16] U. Turaga, C. Song, Catal. Today 86 (2003) 129.
[17] A. Wang, Y. Wang, T. Kabe, Y. Chen, A. Ishihara, W. Qian, P. Yao, J. Catal. 210 (2002) 319.
[18] A. Sampieri, S. Pronier, J. Blanchard, M. Breysse, S. Brunet, K. Fajerwerg, C. Louis, G. Pérot, Catal. Today 107/108 (2005) 537.
[19] L. Vradman, M. Landau, M. Herskowitz, V. Ezersky, M. Talianker, S. Nikitenko, Y. Koltypin, A. Gedanken, J. Catal. 213 (2003) 163.
[20] A. Taguchi, F. Schuth, Micropor. Mesopor. Mater. 77 (2005) 1.
[21] G. Murali Dhar, G. Muthu Kumaran, M. Kumar, K. Rawat, L. Sharma, B. Raju, K. Rama Rao, Catal. Today 99 (2005) 309.
[22] G. Muthu Kumaran, S. Garg, K. Soni, M. Kumar, L. Sharma, G. Murali Dhar, K. Rama Rao, Appl. Catal. A 305 (2006) 123.
[23] O. Gutiérrez, G. Fuentes, C. Salcedo, T. Klimova, Catal. Today 116 (2006) 485.
[24] T. Klimova, J. Reyes, O. Gutiérrez, L. Lizama, Appl. Catal. A 335 (2008) 159.
[25] O. Gutiérrez, K. Romero, G. Fuentes, T. Klimova, Stud. Surf. Sci. Catal. 162 (2006) 355.
[26] O. Gutiérrez, F. Pérez, C. Salcedo, G. Fuentes, X. Bokhimi, T. Klimova, Stud. Surf. Sci. Catal. 165 (2007) 803.
[27] T. Klimova, L. Peña, L. Lizama, C. Salcedo, O. Gutierrez, Ind. Eng. Chem. Res. 48 (2009) 1126.
[28] F. Dumeignil, K. Sato, M. Imamura, N. Matsubayashi, E. Payen, H. Shimada, Appl. Catal. A 315 (2006) 18.
[29] A. Dugulan, High-Pressure Sulfidation of Hydrotreating Catalysts, Genesis and properties of the Active Phase, IOS Press, Amsterdam, 2008. p. 176.
[30] F. Sánchez, J. Ramírez, R. Cuevas, A. Gutiérrez, C. Fernández, Ind. Eng. Chem. Res. 48 (2009) 1178.
[31] D. Zhao, Q. Huo, J. Feng, B. Chmelka, G. Stucky, J. Am. Chem. Soc. 120 (1998) 6024.
[32] C. Pophal, F. Kameda, K. Hoshino, S. Yoshinaka, K. Segawa, Catal. Today 39 (1997) 21.
[33] F. Bataille, J. Lemberton, P. Michaud, G. Pérot, M. Vrinat, M. Lemaire, E. Schulz, M. Breysse, S. Kasztelan, J. Catal. 191 (2000) 409.
[34] M. Houalla, N. Nag, A. Sapre, D. Broderick, B. Gates, AIChE J. 24 (1978) 1015.
[35] Y. Wang, Z. Sun, A. Wang, L. Ruan, M. Lu, J. Ren, X. Li, C. Li, Y. Hu, P. Yao, Ind. Eng. Chem. Res. 43 (2004) 2324.
[36] J. Kim, X. Ma, C. Song, Energy Fuels 19 (2005) 353.
[37] N. Kagami, B. Vogelaar, A. van Langeveld, J. Moulijn, Appl. Catal. A 293 (2005) 11.
[38] J. Chen, H. Yang, Z. Ring, Catal. Today 98 (2004) 227.
[39] P. Da Costa, C. Potvin, J. Manoli, J. Lemberton, G. Pérot, G. Djéga-Mariadassou, J. Mol. Catal. A 184 (2002) 323.
[40] O. Gutiérrez, E. Ayala, I. Puente, T. Klimova, Chem. Eng. Commun. 196 (2009) 1163.
[41] O. Gutiérrez, D. Valencia, G. Fuentes, T. Klimova, J. Catal 249 (2007) 140.
[42] O. Gutiérrez, F. Pérez, G. Fuentes, X. Bokhimi, T. Klimova, Catal. Today 130 (2008) 292.
[43] Z. Liu, Y. Chen, J. Catal. 177 (1998) 314.
[44] C. Williams, J. Ekerdt, J. Jehng, F. Hardcastle, A. Turek, I. Wachs, J. Phys. Chem. 95 (1991) 8781.
[45] C. Williams, J. Ekerdt, J. Jehng, F. Hardcastle, I. Wachs, J. Phys. Chem. 95 (1991) 8791.
[46] R. López-Cordero, F. Gil-Llambias, A. López-Agudo, Appl. Catal. 74 (1991) 125.
[47] J. Ramírez, R. Cuevas, P. Castillo, M. Rojas, T. Klimova, Bulg. Chem. Commun. 30 (1998) 207.
[48] C. Louis, M. Che, M. Anpo, J. Catal. 141 (1993) 453.
[49] P. Arnoldy, J. van den Heijkant, G. de Bok, L. Moulijn, J. Catal. 92 (1985) 35.
[50] E. Hensen, P. Kooyman, Y. van der Meer, A. van der Kraan, V. de Beer, J. van Veen, R. van Santen, J. Catal. 199 (2001) 224.
[51] S. Kasztelan, H. Toulhoat, J. Grimblot, J. Bonnelle, Appl. Catal. 13 (1984) 127.
[52] H. Shimada, Catal. Today 86 (2003) 17.
[53] N. Topsøe, H. Topsøe, J. Catal. 84 (1983) 386.
[54] H. Topsøe, B. Clausen, Appl. Catal. 25 (1986) 273.
[55] S. Bouwens, F. van Zon, M. van Dijk, A. van der Kraan, V. de Beer, J. van Veen, D. Koningsberger, J. Catal. 146 (1994) 375.
[56] P. Moses, B. Hinnemann, H. Topsøe, J. Nørskov, J. Catal. 268 (2009) 201.
[57] S. Eijsbouts, L. van den Oetelaar, R. van Puijenbroek, J. Catal. 229 (2005) 352.
[58] G. Berhault, M. De la Rosa, A. Mehta, M. Yácaman, R. Chianelli, Appl. Catal. A 345 (2008) 80.
[59] P. Da Silva, N. Marchal, S. Kasztelan, Stud. Surf. Sci. 106 (1997) 353.
[60] K. Soni, K. Mouli, A. Dalai, Catal. Lett. 136 (2010) 116.
[61] V. Sundaramurthy, I. Eswaramoorthi, A. Dalai, J. Adjaye, Micropor. Mesopor. Mater. 111 (2008) 560.
[62] J. Lauritsen, M. Nyberg, J. Nørskov, B. Clausen, H. Topsøe, E. Lægsgaard, F. Besenbacher, J. Catal. 224 (2004) 94.
[63] C. Song, X. Ma, Appl. Catal. B 41 (2003) 207.
[64] J. Lauritsen, J. Kibsgaard, G. Olesen, P. Moses, B. Hinnemann, S. Helveg, J. Nørskov, B. Clausen, H. Topsøe, E. Lægsgaard, F. Besenbacher, J. Catal. 249 (2007) 220.
[65] S. Cristol, J. Paul, E. Payen, D. Bougeard, F. Hutschka, S. Clémendot, J. Catal. 224 (2004) 138.
[66] V. Vanrysselberghe, G. Froment, Ind. Eng. Chem. Res. 37 (1998) 4231.